ROYAL SOCIETY OF CHEMISTRY

COMMUNICATION

Nanoporous TiO₂ nanoparticle assemblies with mesoscale morphologies: nano-cabbage *versus* sea-anemone†

Masih Darbandi,*[a] Tesfaye Gebre,[b] Lucas Mitchell,[c] William Erwin,[c] Rizia Bardhan,[c] M. Douglas Levan,[c] Mogus D. Mochena[b] and James H. Dickerson*[a]

We report the novel synthesis of nanoporous TiO₂ nanoparticle ensembles with unique mesoscale morphologies. Constituent nanoparticles evolved into multifaceted assemblies, exhibiting excellent crystallinity and enhanced photocatalytic activity compared with commercial TiO₂. Such materials could be exploited for applications, like organic pollutant degradation.

Existing energy generation and energy conversion challenges and potential applications in environmentally friendly processes, such as pollutant remediation, have driven contemporary research on novel materials that possess characteristics that could be exploited. Several factors, including crystalline phase, crystallite size, specific surface area, and porous structure, have important effects on the photocatalytic activity.[1–3] Thus, a key challenge in this field is the achievement of control over the size and shape of nanostructures, which can strongly affect their structural characteristics and, hence, their physiochemical properties. Among the materials that are being investigated in photocatalysis, TiO₂ remains among the most widely studied because of its low-cost, ease in handling, resistance to photochemical and chemical erosion, non-toxicity, high activity, and durability. Further, TiO₂ is used in other energy devices, such as dye sensitized solar cells, lithium ion batteries, and sensors.[4–13] Notably, TiO₂-based photocatalysis has potential for removing environmental pollutants in wastewater, polluted air, among others, an important device characteristic for water purification in the developing world.[14–18]

Various chemical synthesis methods have been developed for fabricating the TiO₂ nanomaterials, including sol–gel, hydrolysis, precipitation and solvothermal methods.[19–24] For the synthesis of porous TiO₂ nanoparticle (NP) architectures, templates have been used, including hard templates (like porous silica or latex spheres, *etc.*) and soft templates (like triblock copolymers).[25–38] Zhan and collaborators fabricated TiO₂ hollow fibres with mesoporous structure by combining a sol–gel process with a two-capillary spinneret electrospinning technique, using a triblock copolymer as a pore-directing agent.[1] Peng and collaborators prepared mesoporous TiO₂ nanopowders with high specific surface areas and anatase phase by using cetyltrimethylammonium bromide (CTAB) as a surfactant-directing and pore-forming agent.[39] However, after many of the aforementioned syntheses, the template must be removed from the sample to make the pores accessible. This has been achieved by thermal treatment (calcination). Calcination processes mostly lead to the partial or complete collapse of the porous structure during the template removal process and, thus, result in the decrease of the porosity. In addition, some templates cannot be removed completely by thermal treatment because of their tight binding to the materials. Recently, the synthesis of hierarchical structures of porous TiO₂ has been reported. In this and other similar cases, complicated non-scalable synthesis procedures were used. In each of these examples, the resultant TiO₂ materials were amorphous, and post-synthesis treatments were required to obtain crystalline nanostructures.[40–44] Thus, the development of simple, low-cost methods to synthesize such porous materials remains a challenge for scalable material preparation and applications. Herein, nanoporous TiO₂ nanostructures of tunable morphology have been synthesized by a surfactant-free, convenient, and low-cost solvothermal technique. The pore volume, Brunauer–Emmett–Teller (BET) surface area, and the pore diameter distributions of the nanostructures were tuned by adjusting synthesis parameters. The effects of BET surface area, pore volume, and pore size on the photocatalytic activity were studied through the photodegradation of methylene blue (MB) dye and compared favourably with commercially available P25 TiO₂.

[a]*Department of Physics, Brown University, Providence, RI, USA. E-mail: Masih_Darbandi@Brown.edu; James_Dickerson@Brown.edu*

[b]*Department of Physics, Florida A&M University, Tallahassee, FL, USA*

[c]*Department of Chemical and Biomolecular Engineering, Vanderbilt University, Nashville, TN, USA*

To investigate the influence of the experimental parameters on the morphology and nanostructure of the TiO_2, we tuned the synthesis parameters individually. The most obvious effect was observed as the duration of the solvothermal process was tuned. The structural development of the various nano-assemblies was assessed by transmission electron microscopy (TEM); representative images of the nanostructures are presented in Fig. 1 and 2. Fig. 1 depicts TEM images of the as-prepared TiO_2 nano-assemblies, synthesized during a 6 h solvothermal reaction. Under high magnification, these nanostructures appear to comprise multiple faceted platelets, assembled into an object that appears like bundled *cabbage* with diameter around 100 nm. Complementary X-ray diffraction (XRD) measurements of these nano-assemblies confirmed that the materials possessed good crystallinity (Fig. 1d). The diffraction peaks of the so called *nano-cabbage* assembly structures were indexed to the anatase phase of TiO_2 (JCPDS 21-1272). No diffraction peaks associated with rutile or brookite TiO_2 phases were observed, confirming the purity of the TiO_2 nano-assemblies. We estimated the average crystallite sizes of anatase NPs by using the Scherrer formula. The average crystallite sizes of TiO_2 were estimated from the (101) diffraction peak was 15 nm. Comparing with the TEM images, this could be size of single component in the nano-assembly.

We observed dramatic differences in the morphology of the nano-assemblies when shorter solvothermal synthesis times were employed. The mesostructure that was observed in the TEM images of the materials (Fig. 2), which corresponded to a shorter 2 h solvothermal synthesis reaction, were quite distinct from the aforementioned *nano-cabbage* samples. Collections of tendril-like structures and assemblies were observed,
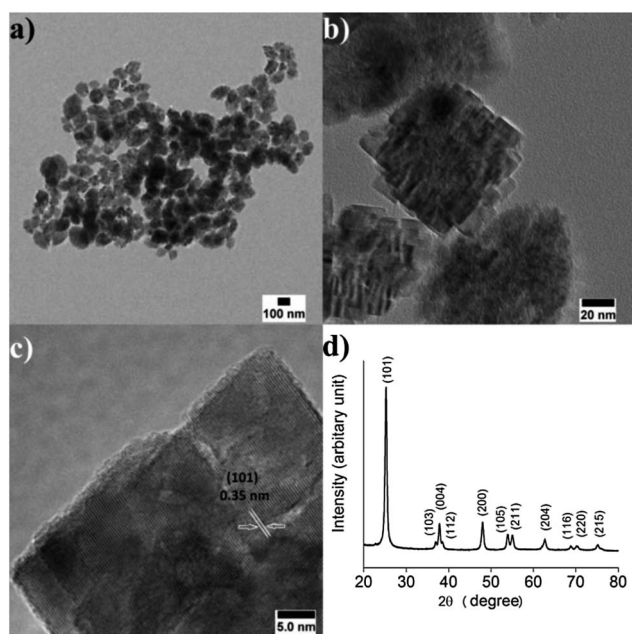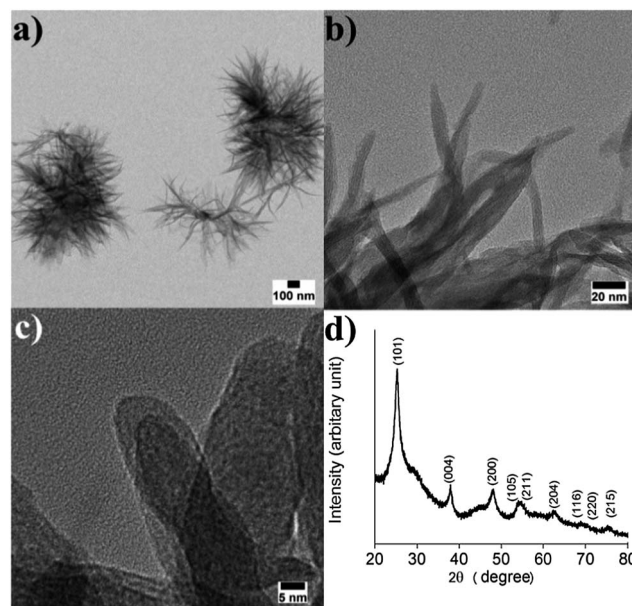

Fig. 2 (a–c) TEM micrographs of different magnifications and (d) XRD spectrum of our TiO_2 assembly that corresponded to a 2 h solvothermal synthesis. This nanostructure was characterized as having *sea-anemone* morphology.

comprised of long, TiO_2 nanofibers that branched outward from a central location. High resolution TEM micrographs of these structures, called *sea-anemone* nano-assemblies, are depicted in Fig. 2b and c. The primary particle dimensions were ~10 nm in diameter and a few hundred nm in length; the overall nano-assembly size was ~0.5 μm, as identified from the TEM images. Thus, the comparative TEM overviews suggest that the shorter solvothermal duration had a strong impact on the synthesis. The XRD pattern of this assembly (Fig. 2d) showed diffraction peaks that correspond to the planes of anatase TiO_2. Average grain sizes of the products have been estimated from the full width at half-maximum of the respective XRD patterns with the Scherrer's formula, which was 12 nm. This diameter could be related to the thickness of single component in the nano-assembly which is in good agreement with TEM images. Both samples showed similar patterns (Fig. 1d and 2d) with peaks corresponding to the (101), (004), (200), (105), (211), (204) and (215) planes of anatase. XRD peaks are intense and narrower in case of cabbage nano-assembly, indicating the formation of greater TiO_2 crystallites and enhancement of crystallization. This conclusion also is supported by the lack of strong, definitive lattice fringes in the TEM images.

The morphologies of both nanostructures (*sea-anemone* and *nano-cabbage*) comprise the assembly of multiple nanoscale facets emerging from a centrally located nucleation and growth sites. In the case of the *sea-anemone* assembly, the shorter solvothermal synthesis time resulted in thin elongated structures, possessing high surface area and porosity. However, in the case of the *nano-cabbage*, the longer solvothermal synthesis yielded considerably thicker structures and lower porosity. The evolution of the shape and organization of the nanomaterials was attributed to Ostwald ripening. To confirm the Ostwald

Fig. 1 (a–c) TEM micrographs of different magnifications and (d) XRD spectrum of our TiO_2 assembly that corresponded to a 6 h solvothermal synthesis. This nanostructure was characterized as having *nano-cabbage* morphology.

ripening effect, a control experiment was conducted at longer solvothermal durations than previously employed, with all other reaction conditions kept constant (ESI, S1†). No obvious effects on the morphology of final product were observed. However, the net diameters of the particles increased with solvothermal duration. Also, the amount of water was varied, maintaining the other synthesis conditions; no substantial effect was observed on the resultant nanomaterials (ESI, S2 and S3†). Yet, in the absence of water, small, cubic nanoparticles were formed (ESI, S4†).

To compare the porosity of final products, nitrogen adsorption–desorption experiments were conducted. Fig. 3 exhibit the nitrogen adsorption–desorption isotherms and the corresponding Barrett–Joyner–Halenda (BJH) pore diameter distribution measurements. *Sea-anemone* nanostructures exhibited well-defined adsorption characteristics at a high relative pressure (P/P_0); the associated curve reflects a typical type-II isotherm with a small hysteresis loop (according to IUPAC nomenclature). The BJH pore size distribution obtained from the adsorption branch also revealed that the majority of pores in the *sea-anemone* assembly were ∼1.6 nm. For the *nano-cabbage* assembly and the P25 TiO$_2$ NP, no obvious hysteresis loops were seen in the corresponding isotherms. The standard multipoint Brunauer–Emmett–Teller (BET) method was used to calculate the surface area of the samples. BET surface area of the *sea-anemone*, *nano-cabbage* and P25 are 264, 61 and 53 m^2 g^{-1} respectively. Notably, the specific surface areas of the *sea-anemone* assembly were 5 times higher than that of P25. This implies that the catalytic performance of *sea-anemone* assembly may be superior to the other TiO$_2$ because of the larger quantity of adsorption sites for interacting species.

The photocatalytic properties of TiO$_2$ NPs have been studied in detail;[44–50] TiO$_2$ NPs and nanoparticle ensembles with large BET surface area and porous structure are expected to exhibit enhanced photocatalytic properties because the large specific surface area of the nanostructure possesses many active sites

such that substances can be adsorbed in large quantities onto the TiO$_2$ surface. The complementary high porosity facilitates pollutant access to those catalytic sites, and the subsequent adsorption and decomposition. The photocatalytic activity of our nano-assemblies was determined by the decomposition rate of MB (measuring the amount of MB that remains within solutions that are exposed to UV illumination at regular intervals). For comparison, the results from the P25 are shown in Fig. 4a. UV light irradiation is needed for the photodecomposition of the MB organic dye, which led to the generation of excited electrons in the conduction band and holes in the valence band (see ESI†). The photogenerated charge carriers reacted with oxygen and water from the environment to produce active oxygen and radical species, which decomposed MB into CO$_2$ and H$_2$O. Further, since this phenomenon took place at the material's surface, the accessibility and interaction of MB with the surface must be high and must be directly linked to the porosity.
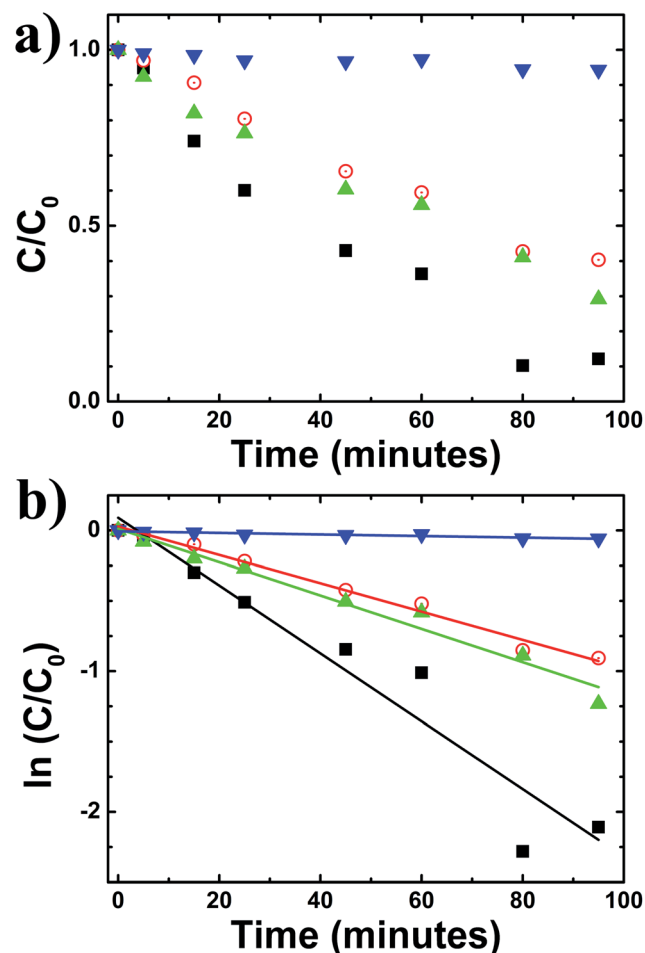
Fig. 4 (a) Graphs of photocatalytic activities for MB decomposition: TiO$_2$ *sea-anemone* nano-assembly (black filled squares), TiO$_2$ *nano-cabbage* assembly (red open circle), P25 (green filled triangle) and MB with no catalysis (blue filled inverted triangle). (b) Graphs of the apparent pseudo-first-order linear transform, ln(C/C_0), *versus* time for the aforementioned TiO$_2$ *sea-anemone* nano-assembly ($R^2 = 0.924$), TiO$_2$ *nano-cabbage* assembly ($R^2 = 0.986$), P25 ($R^2 = 0.970$), and MB with no catalysis ($R^2 = 0.868$).
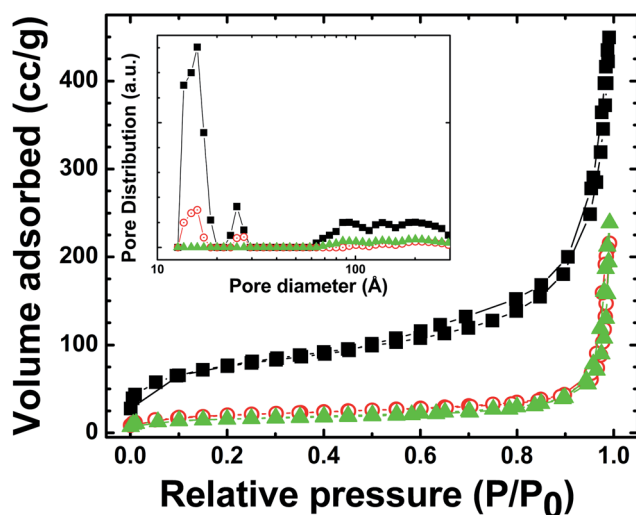

Fig. 3 Nitrogen adsorption–desorption isotherm and (inset) BJH pore-size distribution of *sea-anemone* assembly (black squares), *nano-cabbage* assembly (red circle) and P25 (green triangle).

The photodegradation kinetics of MB is described according to the pseudo-first-order equation as given by eqn (1):

$$\ln(C/C_0) = -Kt \qquad (1)$$

in which C_0 is MB initial concentration, C is the residual concentration of MB at reaction time t, t is the reaction time, and K is the pseudo-first-order rate constant. By plotting $\ln(C/C_0)$ as a function of time t (Fig. 4b) and fitting a linear regressions to that data, we obtained for each sample the K (min^{-1}) constant from the slopes of the fitted straight lines. K was 0.024 min^{-1}, 0.010 min^{-1}, and 0.012 min^{-1} for the *sea-anemone* assembly, the *nano-cabbage* assembly, and P25, respectively. The value for the *sea-anemone* assembly confirms that its activity for photodegradation of MB is the highest among the analyzed materials. Comparing the P25 with our as-synthesized nano-assemblies (*nano-cabbage* & *sea-anemone*), the sample with a higher BET surface area (*sea-anemone*) exhibited enhanced photocatalytic activity, even though P25 had a specific surface area, like the *nano-cabbage* assembly. This meant that samples with higher BET surface area enabled more MB molecules to contribute to the photocatalysis.

In summary, nanoporous anatase TiO$_2$ assemblies were prepared through a facile, low cost, and reproducible solvothermal synthesis. TEM images showed the range of achievable morphologies through this approach, depending on the solvothermal duration under otherwise identical reaction conditions. The obtained *sea-anemone* and *nano-cabbage* morphologies possessed BET specific surface areas of 264 and 61 m^2 g^{-1}, respectively. Our photocatalytic measurements confirmed that the activity is more efficient when the specific surface area was higher, with pores completely accessible to water, oxygen, and adsorbate species. Importantly, the photocatalytic activities of nanoporous *sea-anemone* TiO$_2$ assembly were found to be much better than that of commercial P25 TiO$_2$. These novel structures are promising candidates to replace traditional nanoparticle-based catalysis schemes. The new synthesis approach could be extended to the fabrication of other transition metal-based mesoscale, nanoporous materials.

Acknowledgements

Notes and references

1 S. Zhan, D. Chen, X. Jiao and C. Tao, *J. Phys. Chem. B*, 2006, **110**, 11199–11204.

2 M. Wen, M. Cheng, S. Zhou, Q. Wu, N. Wang and L. Zhou, *J. Phys. Chem. C*, 2012, **116**, 11702–11708.

3 Y. Lai, M. Meng, Y. Yu, X. Wang and T. Ding, *Appl. Catal., B*, 2011, **105**, 335–345.

4 J. Zheng, G. Li, X. Ma, Y. Wang, G. Wu and Y. Cheng, *Sens. Actuators, B*, 2008, **133**, 374–380.

5 H.-G. Yun, J. H. Park, B.-S. Bae and M. G. Kang, *J. Mater. Chem.*, 2011, **21**, 3558–3561.

6 Z. Yong, Z. Jin, T. Shuxin, W. Lifang, J. Lei and Z. Daoben, *Nanotechnology*, 2006, **17**, 2090–2097.

7 Y. Wu, *Sens. Actuators, B*, 2009, **137**, 180–184.

8 H. Wang, Y. Bai, Q. Wu, W. Zhou, H. Zhang, J. Li and L. Guo, *Phys. Chem. Chem. Phys.*, 2011, **13**, 6977–6982.

9 H. Tian, L. Hu, C. Zhang, L. Mo, W. Li, J. Sheng and S. Dai, *J. Mater. Chem.*, 2012, **22**, 9123–9130.

10 X. Shu, Y. Chen, H. Yuan, S. Gao and D. Xiao, *Anal. Chem.*, 2007, **79**, 3695–3702.

11 S. W. Oh, S.-H. Park and Y.-K. Sun, *J. Power Sources*, 2006, **161**, 1314–1318.

12 H.-G. Jung, S. W. Oh, J. Ce, N. Jayaprakash and Y.-K. Sun, *Electrochem. Commun.*, 2009, **11**, 756–759.

13 Y. J. Choi, Z. Seeley, A. Bandyopadhyay, S. Bose and S. A. Akbar, *Sens. Actuators, B*, 2007, **124**, 111–117.

14 Z. Zhang, D. Xu, M. Shen, D. Wu, Z. Chen, X. Ji, F. Li and Y. Xu, *Water Sci. Technol.*, 2011, **63**, 424–431.

15 Y. Yang, H. Wang, J. Li, B. He, T. Wang and S. Liao, *Environ. Sci. Technol.*, 2012, **46**, 6815–6821.

16 J. Wang, F. Y. Wen, Z. H. Zhang, X. D. Zhang, Z. J. Pan, P. Zhang, P. L. Kang, J. Tong, L. Wang and L. Xu, *J. Photochem. Photobiol., A*, 2006, **180**, 189–195.

17 C.-N. Kuo, H.-F. Chen, J.-N. Lin and B.-Z. Wan, *Catal. Today*, 2007, **122**, 270–276.

18 M. Y. Ghaly, T. S. Jamil, I. E. El-Seesy, E. R. Souaya and R. A. Nasr, *Chem. Eng. J.*, 2011, **168**, 446–454.

19 Z. Wang, L. Shi, F. Wu, S. Yuan, Y. Zhao and M. Zhang, *Nanotechnology*, 2011, **22**, 275502.

20 H. Wang, P. Liu, X. Cheng, A. Shui and L. Zeng, *Powder Technol.*, 2008, **188**, 52–54.

21 S. Mahata and D. Kundu, *Mater. Sci.*, 2009, **27**, 463–470.

22 D. P. Macwan, P. N. Dave and S. Chaturvedi, *J. Mater. Sci.*, 2011, **46**, 3669–3686.

23 K. Lee, N. H. Leea, S. H. Shin, H. G. Lee and S. J. Kim, *Mater. Sci. Eng., B*, 2006, **129**, 109–115.

24 I. Gonzalo-Juan, J. R. McBride and J. H. Dickerson, *Nanoscale*, 2011, **3**, 3799–3804.

25 L. Zhao and J. Yu, *J. Colloid Interface Sci.*, 2006, **304**, 84–91.

26 Z. Zhang, F. Zuo and P. Feng, *J. Mater. Chem.*, 2010, **20**, 2206–2212.

27 X. Zhang, G. Zhou, J. Xu, G. Bai and L. Wang, *J. Solid State Chem.*, 2010, **183**, 1394–1399.

28 H. S. Yun, K. Miyazawa, H. S. Zhou, I. Honma and M. Kuwabara, *Adv. Mater.*, 2001, **13**, 1377–1380.

29 L. Yuan, S. Meng, Y. Zhou and Z. Yue, *J. Mater. Chem. A*, 2013, **1**, 2552–2557.

30 D.-H. Yu, X. Yu, C. Wang, X.-C. Liu and Y. Xing, *ACS Appl. Mater. Interfaces*, 2012, **4**, 2781–2787.

31 G. Tang, S. Liu, H. Tang, D. Zhang, C. Li and X. Yang, *Ceram. Int.*, 2013, **39**, 4969–4974.

32 L. Szymanski, P. Surolia, O. Byrne, K. R. Thampi and C. Stubenrauch, *Colloid Polym. Sci.*, 2013, **291**, 805–815.

33 P. Li, C.-F. Zeng, L.-X. Zhang and N.-P. Xu, *J. Inorg. Mater.*, 2008, **23**, 49–54.

34 J. Li, X. Shia, L. Wang and F. Liu, *J. Colloid Interface Sci.*, 2007, **315**, 230–236.

35 M. C. Kimling and R. A. Caruso, *J. Mater. Chem.*, 2012, **22**, 4073–4082.

36 S. Guo, Z. Wu, H. Wang and F. Dong, *Catal. Commun.*, 2009, **10**, 1766–1770.

37 S. Chu, L. Luo, J. Yang, F. Kong, S. Luo, Y. Wang and Z. Zou, *Appl. Surf. Sci.*, 2012, **258**, 9664–9667.

38 S.-W. Choi, J. Y. Park, C. Lee, J. G. Lee and S. S. Kim, *J. Am. Ceram. Soc.*, 2011, **94**, 1974–1977.

39 T. Y. Peng, D. Zhao, K. Dai, W. Shi and K. Hirao, *J. Phys. Chem. B*, 2005, **109**, 4947–4952.

40 J. Wang, Y. Zhou and Z. Shao, *Electrochim. Acta*, 2013, **97**, 386–392.

41 F. Sauvage, F. Di Fonzo, A. L. Bassi, C. S. Casari, V. Russo, G. Divitini, C. Ducati, C. E. Bottani, P. Comte and M. Graetzel, *Nano Lett.*, 2010, **10**, 2562–2567.

42 F. Sauvage, D. Chen, P. Comte, F. Huang, L.-P. Heiniger, Y.-B. Cheng, R. A. Caruso and M. Graetzel, *ACS Nano*, 2010, **4**, 4420–4425.

43 N. Huang, Y. Xie, B. Sebo, Y. Liu, X. Sun, T. Peng, W. Sun, C. Bu, S. Guo and X. Zhao, *J. Power Sources*, 2013, **242**, 848–854.

44 D. Chen, F. Huang, Y.-B. Cheng and R. A. Caruso, *Adv. Mater.*, 2009, **21**, 2206–2210.

45 D. Y. C. Leung, X. Fu, C. Wang, M. Ni, M. K. H. Leung, X. Wang and X. Fu, *ChemSusChem*, 2010, **3**, 681–694.

46 W.-J. Ong, M. M. Gui, S.-P. Chai and A. R. Mohamed, *RSC Adv.*, 2013, **3**, 4505–4509.

47 M. A. Lazar and W. A. Daoud, *RSC Adv.*, 2013, **3**, 4130–4140.

48 W.-J. Ong, L.-L. Tan, S.-P. Chai, S.-T. Yong and A. R. Mohamed, *Nanoscale*, 2014, **6**, 1946–2008.

49 X. Pan, M.-Q. Yang, X. Fu, N. Zhang and Y.-J. Xu, *Nanoscale*, 2013, **5**, 3601–3614.

50 Y. Wang, Q. Wang, X. Zhan, F. Wang, M. Safdar and J. He, *Nanoscale*, 2013, **5**, 8326–8339.